doi: 10.34248/bsengineering.1673237



Research Article

Volume 8 - Issue 5: 1328-1338 / September 2025

CONTACTLESS DETECTION OF ELECTRICAL MACHINE BEARING FAULTS: A RADAR-BASED SOLUTION

Yunus Emre ACAR1*, Salih Bilal CETINKAL2

¹Selcuk University, Faculty of Technology, Department of Electrical and Electronics Engineering, 42075, Konya, Türkiye ²Selcuk University, Faculty of Technology, Department of Metallurgical and Materials Engineering, 42075, Konya, Türkiye

Abstract: Bearing failures represent the most prevalent fault type in electrical machines, potentially leading to catastrophic consequences if not detected early. Conventional detection methods primarily rely on thermal, acoustic, and vibration sensors. Traditional vibration-based techniques have gained widespread adoption due to their stable and straightforward signal-processing capabilities. However, these approaches require direct motor mounting, introducing economic, temporal, and safety inefficiencies. This study presents the first investigation of contactless radar-based detection of bearing faults according to the authors' knowledge. The research employs the absolute value of complex signals derived from quadrature signals recorded by a 24 GHz radar transceiver as the vibration signal. Various defects like corrosion, improper oil levels, and scratches were deliberately introduced to the inner race, outer race, and balls of bearings, establishing 16 distinct fault classes. Classification performance was evaluated using both time-domain statistical features and frequency-domain PSD features. Multiple machine learning algorithms were applied to both approaches, consistently achieving accuracy rates exceeding 98%. This study validates the potential of radar-based systems for bearing fault diagnosis and introduces a novel paradigm for contactless bearing fault detection comprising radar signal data from 880 experiments. The results demonstrate that radar technology offers a promising alternative to traditional contact-requiring methods, enabling efficient and reliable bearing fault classification through non-invasive vibration detection.

Keywords: Bearing, Fault detection, Power spectral density, Radar, Time-domain features

*Corresponding author: Selcuk University, Faculty of Technology, Department of Electrical and Electronics Engineering, 42075, Konya, Türkiye E mail: yacar@selcuk.edu.tr (Y.E. ACAR)

Yunus Emre ACAR Salih Bilal CETINKAL https://orcid.org/0000-0002-6809-9006 https://orcid.org/0000-0001-6212-7670 Received: April 10, 2025 Accepted: June 17, 2025 Published: September 15, 2025

Cite as: Acar YE, Çetinkal SB. 2025. Contactless detection of electrical machine bearing faults: A radar-based solution. BSJ Eng Sci, 8(5): 1328-1338.

1. Introduction

Bearings are critical components in mechanical systems that minimize friction between moving parts, thereby reducing energy loss and increasing load-bearing capacity. These elements significantly enhance the efficiency and durability of systems by supporting rotational or linear motion through rolling elements positioned between inner and outer rings. The importance of bearings is further emphasized by their role in optimizing machine performance and reducing maintenance costs. Considering that approximately 40-50% of mechanical failures in rotating machinery stem from bearing faults, monitoring and maintaining these components plays a vital role (Zhang et al., 2020a). Bearing failures typically result from factors such as inadequate lubrication, contamination, improper installation, overloading, and material fatigue (Brito et al., 2022). These failures can manifest in various forms, including wear, fatigue cracks, corrosion, and surface

Bearing fault detection utilizes various data types, each enabling distinct approaches with inherent advantages and disadvantages. Vibration analysis, owing to its high sensitivity and broad applicability, is prevalent for early fault detection (Qiao et al., 2020; Zhang et al., 2020b; Mueller et al., 2023). However, limitations include the criticality of sensor placement and susceptibility to noise interference. Acoustic emission, leveraging its capacity to capture high-frequency signals, offers advantages in early micro-crack detection, but remains susceptible to ambient noise (Pacheco-Cherrez et al., 2022; Glowacz et al., 2025). Current-based methods, exploiting existing motor current sensors, preclude the need for supplementary hardware; however, sensitivity can diminish in low-speed applications (Kao et al., 2018; Sabir et al., 2019). Thermal imaging, facilitating noncontact measurement of bearing temperature variations, necessitates expensive equipment and may exhibit reduced efficacy in incipient fault stages (Lopez-Perez and Antonino-Daviu, 2017; Mehta et al., 2021). Each approach contributes significantly to bearing fault detection within specific application scenarios and diverse industrial settings.

The detection of bearing faults has seen significant advancements in signal processing approaches and methods over time. Initially, in the earlier decades, basic frequency analysis techniques such as time-domain analyses and the Fast Fourier Transform (FFT) were employed. As the field progressed, the 1980s witnessed



analysis techniques. Moving into the 1990s, more sophisticated signal processing and artificial intelligence methods, including wavelet analysis and neural networks, began to be utilized. In the subsequent years, adaptive signal processing techniques like Empirical Mode Decomposition (EMD) and the Hilbert-Huang Transform gained prominence (Akar et al., 2015). Recently, deep learning-based approaches have become increasingly prevalent. For instance, research by (Zhu et al., 2023) demonstrated the effectiveness of deep learning in bearing fault detection. Emerging trends in this area include multi-sensor fusion, transfer learning, and novel deep network architectures. The advantages of these methods include noise suppression capabilities, early fault detection, and automatic feature extraction. In the field of bearing fault diagnosis, both synthetic and experimental data play crucial roles in the development and validation of diagnostic algorithms. Synthetic data, as utilized in various studies, allows researchers to simulate a wide range of fault conditions, providing a controlled environment to test the efficacy of machine learning models (Liu et al., 2020). Experimental data, such as that from the Case Western Reserve University Bearing Data Center, offers real-world insights and is instrumental in validating these models under practical conditions (Smith and Randall, 2015). The primary equipment used in these studies includes vibration sensors like accelerometers and acoustic emission sensors, which are essential for capturing the subtle signals indicative of bearing faults (Karabacak and Özmen, 2022; Ertarğın et al., 2023; Ercire and Ünsal, 2024; Kilic and Acar, 2024). However, contact-based sensors face challenges such as potential misalignment and the introduction of noise due to physical attachment. Non-contact measurement methods, such as laser-based ones, offer a compelling alternative by eliminating these issues, enabling accurate measurements even in challenging-to-access areas. Moreover, radar-based detection systems provide significant advantages over both laser and infrared systems. While laser and infrared technologies are effective in controlled environments, radar technology excels in harsh industrial conditions where dust, fog, vapors, and temperature variations can compromise measurement accuracy (Acar et al., 2021). Radar systems can penetrate protective covers and operate under various lighting conditions, providing measurements over longer distances and through obstructions. Unlike laser systems that require direct line-of-sight and careful surface preparation, radar sensors leverage the Doppler effect for direct velocity measurements while being resistant to electromagnetic interference. Additionally, a single radar sensor can simultaneously monitor multiple points, capturing not only vibration but also velocity, position, and structural deformation across various frequency bands. These capabilities make radar-based systems a more versatile and cost-effective solution for

the development and widespread adoption of envelope

accessibility and environmental resilience are critical concerns.

In this study, we present significant contributions to the field of bearing fault diagnosis through the development of a comprehensive dataset specifically focused on bearing faults. A total of 880 data samples were generated, encompassing a diverse range of fault types. The experiments were conducted using bearings that were deliberately aged or deformed to simulate realistic fault conditions. Notably, the data were collected using a radar-based non-contact measurement system, marking the creation of the first dataset in the literature that encompasses bearing faults detected via radar technology. This pioneering dataset not only provides a valuable resource for future research but also demonstrates, for the first time, that bearing faults can be classified with very high accuracy using radar-based methods. This advancement opens new avenues for noninvasive and precise fault diagnosis in industrial applications. The subsequent sections of this paper will detail the dataset creation process, methodologies employed, and the results obtained, thereby elucidating the significance of this novel approach in the context of bearing fault diagnosis and its potential implications for industrial maintenance practices.

2. Materials and Methods

2.1. Radar-Based Vibration Estimation

The motion detection capability of continuous wave radars represents a fascinating phenomenon with diverse application domains in electrical engineering. The Doppler principle underpins a spectrum of applications, creating a methodological continuum that spans from detecting high-velocity objects like vehicles and aircraft to the subtle monitoring of vital physiological parameters—pulse rates and respiratory patterns—through the minute movements of the chest wall.

In these systems, a high-frequency RF signal generated via an oscillator is typically amplified through a power amplifier before radiating toward the target through an appropriate antenna. A portion of the oscillator signal, diverted immediately before the amplification stage, is mixed with the reflected signal through a mixer. The resulting low-frequency signal fundamentally represents the differential between transmitted and received signals. This low-frequency component encapsulates the target's motion information and enables target displacement determination after subsequent processing. Modern systems incorporate quadrature receiver sections to circumvent the inherent null point issue (Seflek et al., 2020) due to the trigonometric approaches to extract target displacement information. These radar configurations contain two mixer stages that combine the return signal with signals phase-shifted by 90 degrees from each other, thereby providing two baseband signals with a 90-degree phase difference. The fundamental block diagram of these IQ-demodulated radar structures is illustrated in Figure 1.

continuous monitoring in industrial applications where

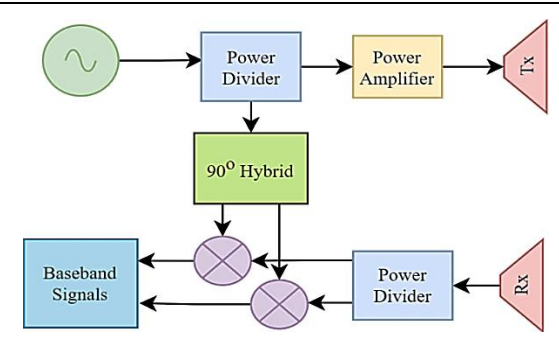


Figure 1. Block scheme of an IQ-demodulated radar.

The baseband signals $b_I(t)$ and $b_Q(t)$ provided by the IQ-demodulated radar structure can be expressed in sinusoidal forms as shown in equations 1 and 2, following elementary DC signal elimination processes. These orthogonal components constitute the fundamental representation of the target's motion characteristics.

$$b_I(t) = \cos\left(\frac{4\pi d_0}{\lambda_c} + \frac{4\pi x(t)}{\lambda_c}\right) = \cos(\theta) \tag{1}$$

$$b_Q(t) = \sin\left(\frac{4\pi d_0}{\lambda_c} + \frac{4\pi x(t)}{\lambda_c}\right) = \sin(\theta)$$
 (2)

In this context, λ_c represents the operational wavelength of the radar, d_0 denotes the static distance between the radar and the target, and x(t) signifies the target's displacement over time. The equations presented in equation 1.a and equation 1.b should theoretically incorporate residual phase noise terms. However, due to common source utilization, these terms become negligible (Gu et al., 2017) resulting in phase information θ being directly proportional to $d_0 + x(t)$.

Among the numerous methodologies proposed for phase information extraction, Differential Arctangent Cross Multiplication (DACM), Extended-DACM, Arctangent Demodulation (AD), and Complex Signal Demodulation (CSD) approaches predominate in practical applications. This study focuses on the CSD approach due to its superior immunity against high DC noise interference (Acar, 2024). This methodology utilizes the baseband signals as real and imaginary components of a complex signal. Following the Fourier transformation applied to this complex-valued signal, the frequency spectrum of the displacement signal is obtained. This spectrum can effectively substitute the vibration spectra traditionally employed in bearing fault diagnostics. The processes of complex signal formation and frequency spectrum generation are delineated in equation 3 and equation 4, respectively.

$$c[n] = b_I[n] + jb_Q[n] = e^{j\left(\frac{4\pi d_0}{\lambda_c} + \frac{4\pi x[n]}{\lambda_c}\right)}$$
 (3)

$$C[k] = \frac{1}{N} \sum_{n=0}^{N-1} c[n] e^{-j2\pi kn/N}$$
 (4)

Within this framework, c[n] denotes the complex-valued signal, C[k] represents the spectral information corresponding to the vibration, and N indicates the number of frequency points representing the spectrum.

2.2. Bearing Aging/Deforming Procedure

Bearing failures constitute the majority of motor failures occurring in industrial facilities. Different bearing models are employed based on varying load and operating conditions. This study focuses on 6205ZZ model bearings used in three-phase 1.1kW asynchronous motors. To simulate common bearing failures, bearing components (balls, cage, and outer rings) were supplied by ANADOLU RULMAN İMALAT SANAYİ VE TİCARET A.Ş. (ART). As part of the study, 16 bearings were prepared, including 15 defective bearings and a healthy bearing, to analyze three different failure types specified in Figure 2.

Lubricant Failures (LF): This bearing failure occurs due to the gradual reduction or performance degradation of lubricant within the bearing over time. During assembly, the ART company constructed the bearings with three different lubricant quantities (25%, 50%, and 75%) instead of the standard lubricant amount typically applied to a standard bearing.

Corrosion: Corrosions on the bearings occur with exposure to moisture or water under operating conditions. In this study, bearing components (balls, rings, and cages) were immersed in a laboratory-prepared aggressive acidic solution for a specific duration. After removal, we cleaned the components with alcohol and subjected them to ultrasonic cleaning. Thus, we have created three different corrosion damages: ball corrosion, ring corrosion, and cage corrosion.

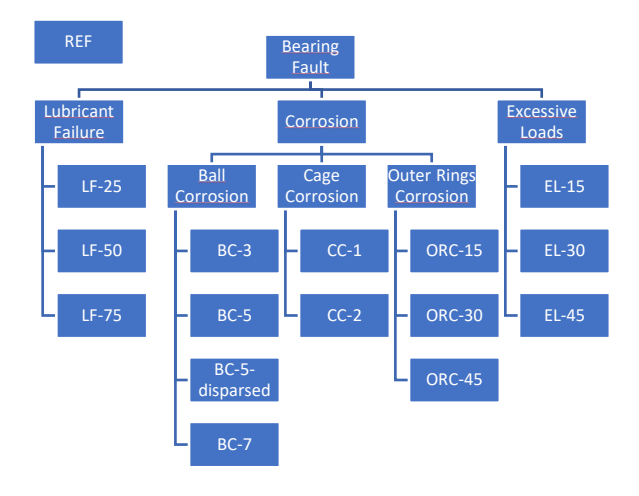


Figure 2. Prepared bearing types.

Ball Corrosion (BC-X): This type of failure occurs when all or some of the nine balls in a bearing are corroded. We have created different damage levels with varying numbers of corroded balls (3, 5, and 7) in each bearing. When assembling the bearings, some were corroded balls (Figure 3.b), and the rest were solid balls (Figure 3.c). The corroded balls were positioned adjacently (BC-3, BC-5, BC-7) or in a dispersed pattern (BC-5-dispersed).

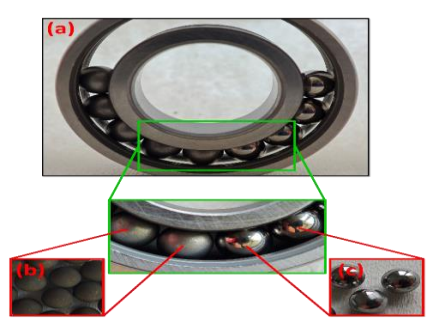


Figure 3. (a) The fabricated ball-corrosion specimen (BC-5), (b) corroded balls, (c) solid balls.

Outer Ring Corrosion (ORC-X): This failure originates from localized corrosion on the bearing's outer ring. We developed corrosion regions with distinct angular widths (15°, 30°, and 45°) on the interior surfaces of the outer rings. In Figure 4.a, the green-marked area represents the surface before acidic solution exposure, while the redmarked area indicates the surface following acidic solution treatment. As an outer ring defect, Figure 4.b is a magnified view of Figure 4.a to better illustrate the ORC-15 fault.

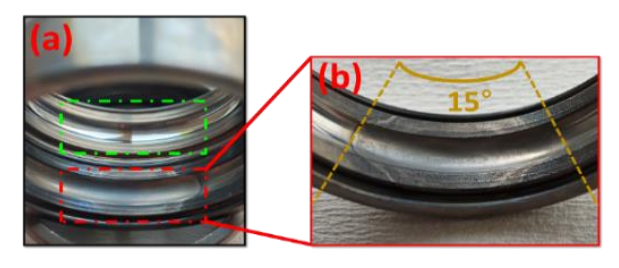


Figure 4. The fabricated outer-ring-corrosion specimen (ORC-15).

Cage Corrosion (CC-X): The wear of the cage surrounding the bearing balls causes these types of failures. We fabricated two distinct levels of failures with varying times the cages were immersed in the acidic solution. Figure 5 show cages of healthy and corroded specimens.



Figure 5. The cages of (a) healthy and (b, c) corroded specimens.

Excessive Load Failures (ELF-X): Wear damage occurs on the outer ring or ball surfaces due to excessive loads. We created three levels of damage by creating wear along different angles (15°, 30°, and 45°) on the ball path on the inner surface of the outer ring. In Figure 6.a, the part marked in green is the surface image where there is no wear, and the part marked in red is the surface image where there is wear. In Figure 6.b, the yellow arrow shows the close-up view of the ball-wear paths.

Following the laboratory creation of these failure mechanisms, the ART assembled the bearings through their standard bearing assembly protocols.

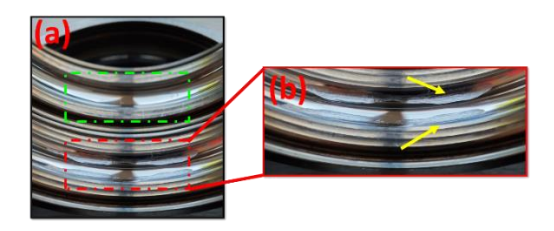


Figure 6. The created wear damage on the outer ring.

2.3. Experimental Setup and Data Acquisition

This study utilizes an experimental setup developed by Piritech to monitor bearing faults. The setup contains a single asynchronous motor coupled with a magnetic powder brake to load the motor. The setup also integrates a motor driver and a magnetic powder brake driver to control the rotational speed and load levels.

We have executed 55 experiments and stored the data for each bearing fault class. The motor operated at eleven equally spaced speed levels between 500 and 1500 rpm, and each speed level included five uniformly distributed load settings from 0 to 2.5 Nm. We have replaced the motor's bearing with an appropriately deformed one for each class.

We employed a straightforward Raspberry Pi-based hardware system to collect the radar data. We transmitted a 24.125 GHz signal toward the motor using the RFspace KLC5 transceiver and gathered the resulting low-frequency return signals. We then digitized the analog baseband signals at a 10 kHz sampling rate with the MCC118 device from Measurement Computing Corporation, saving them to an SD card through the Raspberry Pi. Our data set consists of 880 recordings distributed across 16 fault classes, and each recording contains 300,000 rows with two columns corresponding to the in-phase (I) and quadrature (Q) signals (Acar and Cetinkal, 2025). Figure 7 illustrates the experimental setup.

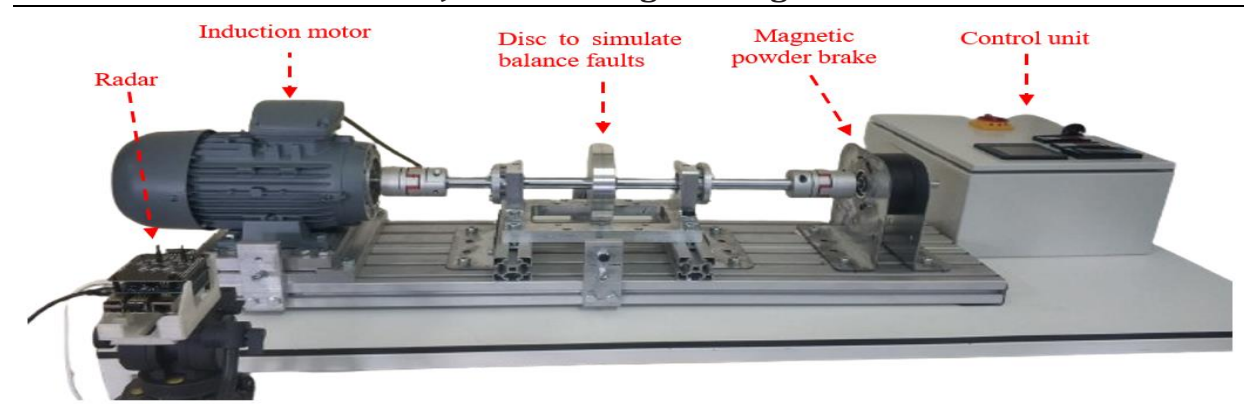


Figure 7. The experimental setup.

2.4. Data Processing

The discrete baseband signals recorded in the time domain constitute the dataset utilized in this research. By integrating these signals through complex signal demodulation techniques, we can effectively capture the micro-displacements of the target. This displacement signal, originating from motor vibrations, reflects the motor's oscillatory behavior in the time domain. The discrete signal, comprising 300.000 samples, is excessively lengthy for direct input into a classifier, necessitating additional feature extraction processes before implementation in machine learning algorithms. In this investigation, we executed feature extraction procedures in both temporal and frequency domains and

conducted comparative analyses of the resultant outcomes.

2.4.1. Time-domain feature extraction

Engineers frequently analyze statistical characteristics of time-domain recordings when classifying bearing faults through vibration signals. Our research leverages 12 proven statistical features (Nayana and Geethanjali, 2017) extracted from the time domain. We first segment the input signal using sliding windows of length L with an overlap ratio O. We then apply all feature extraction techniques to these segments. We calculate the average of features across all segments to create the final feature representation. Figure 8 illustrates this extraction process clearly.

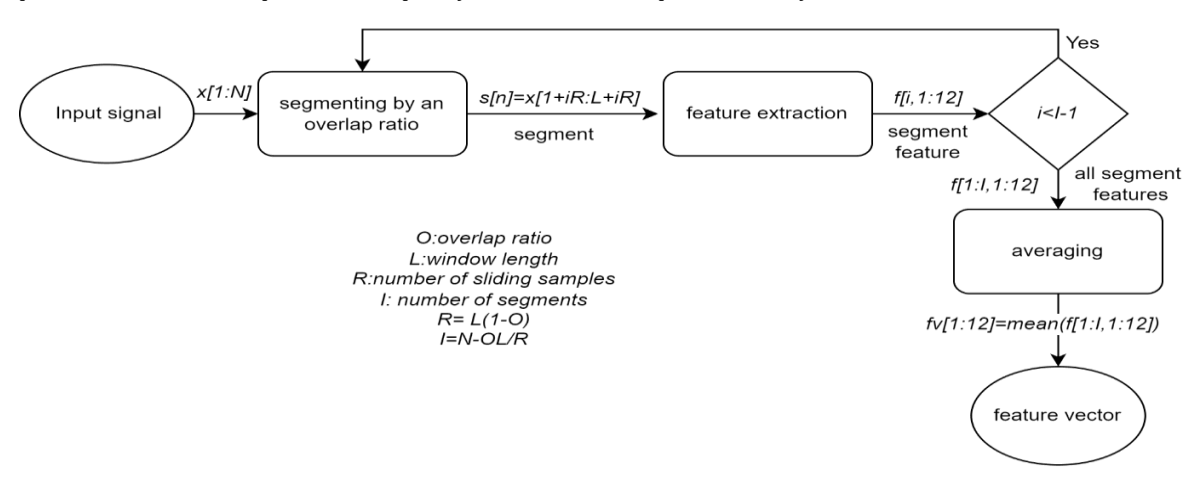


Figure 8. Time-domain feature extraction scheme.

Mean Absolute Value (MAV): This feature provides the mean of absolute values of samples within the segment and is calculated as shown in equation 5.

$$MAV = \frac{1}{L} \sum_{n=1}^{L} |x[n]|$$
 (5)

Energy (E): This feature represents the segment's energy and is calculated as given in equation 6.

$$E = \sum_{n=1}^{L} x[n]^2 \tag{6}$$

Waveform Length (WL): This feature corresponds to the sum of absolute differences between consecutive samples. It represents the sum of absolute first-order derivatives, providing information about the signal's roughness, rate of change, and frequency characteristics for discrete signals. WL is calculated as shown in equation 7.

$$WL = \sum_{n=1}^{L} |x[n] - x[n-1]|$$
 (7)

Willison Amplitude (WA): This feature compares the difference between consecutive samples against a threshold value and counts instances where this difference exceeds the threshold. WA is calculated using equation 8 and 9.

$$WA = \sum_{n=1}^{L} f[x[n] - x[n+1]]$$
 (8)

$$f(x) = \begin{cases} 1 & \text{if } x \ge \varepsilon \\ 0 & \text{otherwise} \end{cases}$$
 (9)

Zero Crossing (ZC): This feature determines the number of zero crossings within the segment. The expression in equation 10 identifies a zero crossing when consecutive values have different signs. To reject low-amplitude oscillations around zero, one can additionally check whether the difference between two samples exceeds a threshold value using the expression provided in equation 11.

$$ZC = \sum_{n=1}^{L} (x[n] \times x[n+1]) < 0$$
 (10)

$$(|x[n] - x[n+1]|) > \varepsilon \tag{11}$$

Slope Sign Change (SSC): This feature calculates the number of slope sign changes in the segment, effectively identifying points where the signal direction changes. These slope sign changes can be determined as shown in equation 12. To exclude minor fluctuations, one can only count instances where the difference between consecutive samples exceeds a threshold value, using the condition specified in equation 11.

$$SSC = \sum_{n=1}^{L} ((x[n+1] - x[n]) \times (x[n] - x[n-1])) < 0$$
 (12)

Root Mean Square (RMS): This feature calculates the square root of the mean square of the segment as given in equation 13.

$$RMS = \sqrt{\frac{1}{L} \sum_{n=1}^{L} x[n]^2}$$
 (13)

Mean (μ) : This feature calculates the average of the segment as given in equation 14.

$$Mean = \mu = \frac{1}{L} \sum_{n=1}^{L} x[n]$$
 (14)

Variance (σ^2) : This feature calculates the squared deviations from the mean value. The average of the squared deviations gives variance. The variance value for each segment is calculated as given in equation 15.

Variance =
$$\sigma^2 = \frac{1}{L} \sum_{n=1}^{L} (x[n] - \mu)^2$$
 (15)

Standard Deviation (STD): This feature calculates the square root of the variance as in equation 16.

$$STD = \sigma = \sqrt{\frac{1}{L} \sum_{n=1}^{L} (x[n] - \mu)^2}$$
 (16)

Skewness (SKW): This property is a measure of the symmetry of a distribution. It is zero for symmetric

distribution. In an unsymmetric distribution, the sign of the skewness value can be positive or negative, depending on whether it is skewed to the right or left. The skewness of a segment is calculated as given in equation 17.

$$SKW = \frac{\frac{1}{L} \sum_{n=1}^{L} (x[n] - \mu)^3}{\sigma^3}$$
 (17)

Kurtosis (KURT): This feature measures the sharpness or flatness of a distribution. The KURT value of a segment as shown in equation 18, provides a quantitative assessment of the signal's distribution shape relative to a normal distribution.

$$KURT = \frac{\frac{1}{L}\sum_{n=1}^{L}(x[n] - \mu)^4}{\sigma^4}$$
 (18)

2.4.2. Power spectral density estimation

Power spectral density is a vital engineering tool that shows how power is distributed across frequency components. Engineers typically use two main approaches to calculate this density. For simple linear systems, parametric methods work well because they're easier to model. However, non-parametric methods like the Welch technique prove more effective where modeling becomes challenging.

The Welch method offers a practical Fourier-based approach to Power Spectral Density (PSD) estimation. The signal is first divided into equal-length segments, making a notable tradeoff: longer segments give better frequency resolution, while shorter ones provide better time resolution. By overlapping these segments, the number of segments is increased without changing their length. Then, the Fourier transform is applied to the segments after windowing to minimize the spectral leakage. Each segment's periodogram $P_m(f)$ is then calculated by squaring its Fourier transform as given in equation 19.

$$P_m(f) \cong \frac{1}{K} \left| \sum_{k=0}^{K-1} x_m(k) e^{\frac{-j2\pi fk}{K}} \right|^2$$
 (19)

Here, K represents the length of the Fourier transform, while $x_m(k)$ denotes the m^{th} segment weighted by a window function w(k). To achieve a specific overlap ratio, we perform a shift-and-window operation on the signal x(k) by sliding R samples at a time, as illustrated in equation 20. This sliding window approach allows us to maintain consistent overlap between adjacent segments while processing the entire signal.

$$x_m(k) \cong w(k)x(k+mR),$$

 $(k=0,1,2,...,K-1,m=0,1,2,...,M-1)$
(20)

The PSD of the entire signal is estimated by averaging the periodograms of all segments, as shown in equation 21. This averaging process helps reduce variance in the spectral estimate and produces a more reliable representation of the signal's frequency characteristics.

$$P_{Welch}(f) = \frac{1}{M} \sum_{m=0}^{M-1} P_m(f)$$
 (21)

2.4.3. Machine learning classifiers and hyperparameters

In this study, we have employed traditional machine learning approaches to classify bearing faults. We tested K-Nearest Neighbors (KNN), Decision Tree (DT), Support Vector Machine (SVM), Linear Discriminant (LD), and several ensemble approaches with various parameters. Table 1 presents the optimal parameters for the best-performing methods, highlighting the configuration that delivered superior classification accuracy in our bearing fault diagnosis system.

Table 1. The ML methods and selected parameters

Method	Parameters		
	Kernel function: linear, quadratic,		
SVM	cubic		
2 A IAI	box constraint level: 1		
	multiclass meth.: one vs one		
	# of neighbors: 1		
KNN	distance metric: Euclidean		
	distance weight: equal		
DT	Max. # of splits: 100		
וע	split criterion: Gini diversity index		
LD	Preset: Linear discriminant		
LD	covariance structure: full		
	Ensemble method: Subspace		
Subspace	learner type: Discriminant		
Discriminant	# of learners:30		
	subspace dimension:65		
	Ensemble method: Subspace		
Cubenaca VNN	learner type: nearest neighbors		
Subspace KNN	# of learners:30		
	subspace dimension:65		

2.5. Performance Evaluation Metrics

When evaluating classification performance, we must understand how accurately a model identifies positive class examples and under what conditions it makes errors. In this context, True Positive (TP) indicates when a model correctly classifies a genuinely positive example

as positive, demonstrating successful detection of target class instances. Conversely, False Positive (FP) occurs when the model incorrectly labels a non-positive example as positive. Finally, a False Negative (FN) happens when the model assigns a positive example to a negative or different class, showing that it missed detecting a positive case it should have captured.

Using these values as shown in equations 22-25, it is common to employ Accuracy, Recall, Precision, and F1-score metrics to assess classification performance. These metrics provide complementary insights into different aspects of the model's effectiveness in correctly identifying and distinguishing between classes.

$$Accuracy = (\Sigma TPs) / (All predictions)$$
 (22)

$$Prec. = TP / (TP + FP) \tag{23}$$

$$Rec. = TP / (TP + FN)$$
 (24)

$$F1-score = 2 x (Prec. x Rec.) / (Prec. + Rec.)$$
 (25)

In multi-class applications, these metrics are calculated on a per-class basis. In this study, we have presented the average of class-specific metrics to evaluate overall model performance. We also assess performance through additional practical considerations like training speed, prediction speed, and model size.

3. Results and Discussion

This section presents the classification results obtained by applying machine learning approaches to features extracted from time-domain analysis and frequencydomain PSD. The performances of different classifiers with these distinct feature sets to diagnose bearing faults are compared.

3.1. PSD-Based Approach

Table 2 presents the performance of various ML approaches with PSD inputs for both validation and test data sets. The performances of the methods are compared through accuracy, precision, recall, and F1 score.

Table 2. Classification performance of ML classifiers with PSD input

	Validation			Test				
ML Meth.	Accuracy	Precision	Decall (0/)	F1 Score	Accuracy	Precision	Decall (0/)	F1 Score
	(%)	(%)	Recall (%)	(%)	(%)	(%)	Recall (%)	(%)
LD	98.9	98.9	98.9	98.9	97.7	97.8	97.7	97.7
Sub. KNN	98.6	98.6	98.6	98.6	98.9	98.9	98.9	98.9
Sub. Disc.	98.5	98.5	98.5	98.5	97.7	97.8	97.7	97.7
Quad. SVM	95.3	95.5	95.3	95.4	94.3	94.5	94.3	94.4
DT	85.5	86.2	85.5	85.8	90.9	91.2	90.9	91.1
KNN	76.9	79.3	76.9	78.1	84.1	85.3	84.1	84.7

According to Table 2 the LD model demonstrates superior performance with 98.86% accuracy on the validation set, while the Subspace KNN model excels on the test set with 98.86% accuracy. The Subspace Discriminant model also shows consistently high performance on both validation (98.48%) and test

(97.73%) sets. A quick assessment based on accuracy clearly distinguishes these three methods from others.

The SVM algorithm exhibits moderate-to-high performance with accuracy rates of 95.33% and 94.32% on validation and test sets respectively, approaching the performance of the top three methods. DT and KNN

algorithms show comparatively lower performance; however, their higher accuracy rates on test sets versus validation sets indicate good generalization capabilities without overfitting issues.

The proximity of precision, recall, and F1 scores to accuracy values across all models suggests a balanced performance distribution among classes. Ensemble methods (Subspace KNN and Subspace Discriminant) outperforming standard algorithms demonstrate their effectiveness in complex classification problems.

Similar performance across methods necessitates additional application-specific selection criteria to determine the optimal approach. Prediction speed, training duration, and model size are the further metrics for real-time applications. Table 3 compares these methods in terms of testing speed, training duration, and model size.

Table 3 Prediction speed, training time, and model size of the models with PSD inputs

-	Prediction	Training		
ML Meth.		0	Model size	
ML Meth.	Speed	Time		
	(obs/sec)	(sec)	5126	
LD	2700	8.62	332 kB	
Sub. KNN	550	176.2	13 MB	
Sub. Disc.	700	168.1	3 MB	
Quad. SVM	840	57.3	3 MB	
DT	6600	15.52	55 kB	
KNN	3000	119.3	838 kB	

Table 3 reveals that the DT algorithm possesses the highest prediction speed, processing 6600 observations per second with just a 15.52-second training period. It also stands out as the most compact model at only 55 kB.

KNN and LD algorithms also show impressive prediction speeds, processing 3000 and 2700 observations per second, respectively. The LD model trains fastest at 8.62 seconds and maintains a compact 332 kB size.

In contrast, the Subspace KNN algorithm exhibits the lowest prediction performance at 550 observations per second and requires the longest training time at 176.2 seconds. It also demands the largest model size of 13 MB. SVM and Subspace Discriminant models show moderate prediction speeds and model sizes.

When evaluating classification metrics and computational performance parameters together, the LD algorithm offers the optimal balance. It achieves high classification performance (98.86% validation and 97.73% test accuracy) while demonstrating superior computational efficiency with 2700 observations processed per second, 8.62-second training time, and compact 332 kB size. Although the Subspace KNN model provides the highest test accuracy (98.86%), its low prediction speed (550 obs/sec), extended training time (176.2 seconds), and large model size (13 MB) create computational resource disadvantages. Despite having the fastest prediction performance (6600 obs/sec) and smallest model size (55 kB), The DT algorithm shows lower classification performance among other models.

3.2 Time-domain features-based approach

This section presents the experimental results of classifying bearing faults utilizing features extracted in the time domain. The features are extracted from the segments with duration of 1 second and an overlap ratio of 25%. Table 4 demonstrates the performance capabilities of the previously dis cussed machine learning methodologies with time-domain features.

Table 4 Classification performance of ML classifiers with time-domain features

	Validation			Test				
ML Meth.	Accuracy	Precision	Recall (%)	F1 Score	Accuracy	Precision	Recall (%)	F1 Score
	(%)	(%)	Recail (%)	(%) (%	(%)	(%)	Recail (%)	(%)
LD	97.9	98.0	97.9	97.8	98.9	99.1	99.0	99.0
Sub. KNN	72.5	72.2	72.5	72.3	60.2	65.7	60.8	61.5
Sub. Disc.	98.4	98.4	98.4	98.3	100.0	100.0	100.0	100.0
Lin. SVM	99.9	99.9	99.9	99.9	100.0	100.0	100.0	100.0
DT	97.0	97.1	97.0	97.0	97.7	98.2	97.7	97.8
KNN	99.5	99.5	99.5	99.5	100.0	100.0	100.0	100.0

Upon examining the results in the validation and test sets presented in Table 5, the SVM algorithm demonstrates superior performance with an accuracy rate of 99.9% in the validation and 100% in the test sets. Similarly, KNN and Subspace Discriminant algorithms achieved 100% accuracy in the test set. LD and DT algorithms provide satisfactory test results with accuracy rates of 98.9% and 97.7%, respectively. The Subspace KNN algorithm, however, shows significantly lower performance with a test accuracy of 60.2%. To evaluate the computational performances, Table 5 provides the prediction speed, training duration, and model size of the methods

operated with time-domain features.

According to Table 5, the Linear Discriminant algorithm stands out with a training duration of 3.1 seconds and a prediction speed of 18,000 observations/second. The DT algorithm also demonstrates efficient performance with a training duration of 13.5 seconds and a prediction speed of 13,000 observations/second. The SVM algorithm has the lowest prediction speed at 960 observations/second. In terms of model size, LD (11 kB) and DT (19 kB) offer the most compact models, while Subspace KNN (2 MB) exhibits the highest storage requirement.

Table 5. Prediction speed, training time, and model size of the models with time-domain features

	Prediction	Training	
ML Meth.	Speed	Time	Model size
	(obs/sec)	(sec)	
LD	18000	3.1	11 kB
Sub. KNN	1500	64.3	2 MB
Sub. Disc.	1800	61.1	215 kB
Lin. SVM	960	44.7	760 kB
DT	13000	13.5	19 kB
KNN	14000	50.7	98 kB

When considering Table 4 and Table 5 together, the performance-efficiency balance of the algorithms becomes more evident. Although SVM, KNN, and Subspace Discriminant algorithms demonstrate superior classification performance, they exhibit different computational efficiency profiles. The Linear Discriminant algorithm presents a remarkable balance with 98.9% test accuracy, the fastest training duration, high prediction speed, and minimal model size. These characteristics make the LD algorithm preferable in resource-constrained environments or real-time applications. The Subspace KNN algorithm, when used with time-domain features, is considered the most disadvantageous option in terms of both performance

and efficiency.

3.3. Overall Evaluation

Table 2 and Table 4 confirm that radar-based systems can effectively diagnose bearing faults through vibration detection. The Linear Discriminant algorithm becomes the most efficient method across both approaches while maintaining high classification accuracy. Subspace Discriminant performs nearly as well as SVM in terms of both classification accuracy and computational efficiency. Despite their computational advantages, DT and KNN algorithms demonstrate significantly lower classification performance in the PSD-based approach than other methods. The Subspace KNN approach performed particularly poorly when using time-domain features.

Although the conventional PSD-based approach achieves high accuracy across various algorithms, it presents disadvantages in training duration, prediction speed, and model size compared to time-domain methods. This efficiency gap primarily stems from the dimensional difference: PSD methods utilize 129 features (representing frequency points across the spectrum), while time-domain approaches require only 12 features. Figure 9 provides a comparative summary of all methods, evaluating classification performance based on validation accuracy and computational efficiency based on prediction speed.

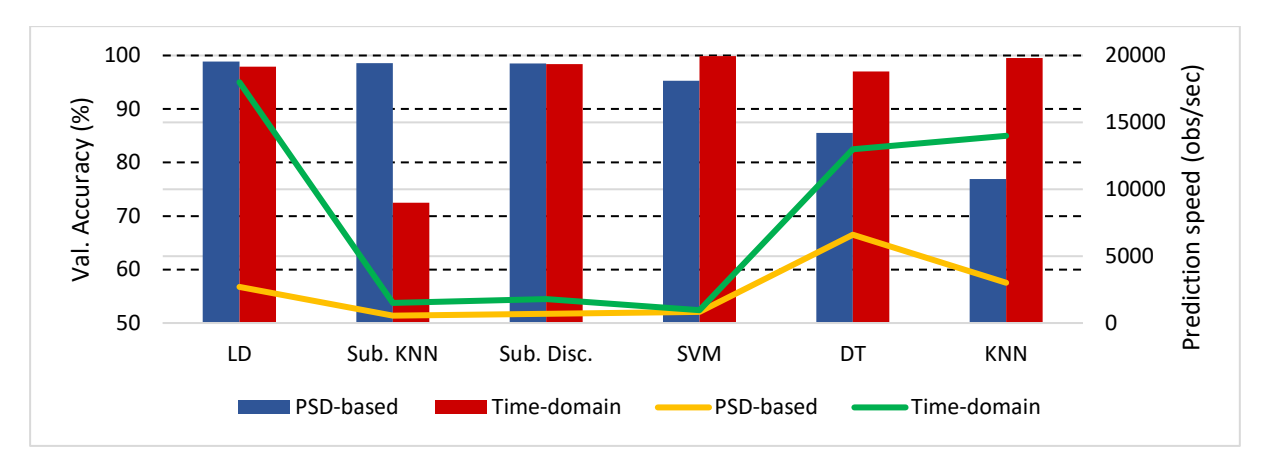


Figure 9 The overall comparison of the methods.

4.Conclusion

This study presents an innovative approach for radar-based diagnosis of bearing failures. Our research demonstrates that a 24 GHz radar system offers a non-contact detection of the bearing faults. Within the scope of this work, we have deliberately induced various defects in the inner race, outer race, and rolling elements of bearings. Corrosion, dust contamination, improper lubrication levels, and scratches are artificially generated with different severity levels and classified using a radar-based system.

PSD estimation and time-domain features with machine learning methodologies enabled the classification of these diverse bearing faults with accuracy exceeding 98%. These findings substantiate the capability of radar-

based diagnostic techniques to differentiate various damage types in bearing components, offering a robust alternative to conventional contact-requiring methods.

Our investigation has contributed to the literature by providing radar signal data from 880 experiments encompassing 16 distinct classes. This dataset constitutes a valuable resource for future research endeavors. This pioneering study presents a new paradigm for non-contact fault diagnosis in bearing maintenance and monitoring processes.

Future research directions should examine the impact of different radar operating frequencies on performance, optimization of detection distance, and system reliability under various environmental conditions. Additionally, integration with real-time monitoring systems and

algorithms for detecting more complex fault types will contribute to advancements in this field.

Author Contributions

The percentages of the authors' contributions are presented below. All authors reviewed and approved the final version of the manuscript.

	Y.E.A.	S.B.Ç.
С	70	30
D	30	70
S	50	50
DCP	50	50
DAI	50	50
L	50	50
W	80	20
CR	50	50
SR	50	50
PM	50	50
FA	0	100

C=Concept, D= design, S= supervision, DCP= data collection and/or processing, DAI= data analysis and/or interpretation, L= literature search, W= writing, CR= critical review, SR= submission and revision, PM= project management, FA= funding acquisition.

Conflict of Interest

The authors declared that there is no conflict of interest.

Ethical Consideration

Ethics committee approval was not required for this study because of there was no study on animals or humans.

Acknowledgements

The authors gratefully acknowledge the ART company for their valuable contribution in supplying the bearing components and for their technical expertise in assembling the artificially aged bearing specimens essential for this research.

References

- Acar YE, Cetinkal SB. 2025. SU RF Sensing Lab. Bearing Fault Diagnosis Dataset. Kaggle. https://www.kaggle.com/datasets/yunusemreacar1/su-rf-sensing-lab-bearing-fault-diagnosis-dataset (accesed date, March 15, 2025).
- Acar YE. 2024. Radar-enabled non-contact speed estimation for rotating electrical machinery. Measurement, 235: 114989.
- Acar YE, Saritas I, Yaldiz E. 2021. An S-band zero-IF SFCW through-the-wall radar for range, respiration rate, and DOA estimation. Measurement, 186: 110221.
- Akar M, Hekim M, Orhan U. 2015. Mechanical fault detection in permanent magnet synchronous motors using equal width discretization-based probability distribution and a neural network model. Turk J Electr Eng Comput Sci, 23: 813–823.
- Gu C, Huang TY, Li C, Lin J. 2017. Microwave and millimeterwave radars for vital sign monitoring. In: Amin MG, editor.

- Radar for Indoor Monitoring. CRC Press, Florida, USA, pp: 199–226.
- Brito LC, Susto GA, Brito JN, Duarte MA. 2022. An explainable artificial intelligence approach for unsupervised fault detection and diagnosis in rotating machinery. Mech Syst Signal Process, 163: 108105.
- Ercire M, Ünsal A. 2024. Asenkron motor eş zamanlı çoklu arızalarının titreşim sinyalleri ile çok etiketli sınıflandırılması. Duzce Univ J Sci Technol, 12: 1296–1314.
- Ertarğın M, Yıldırım Ö, Orhan A. 2023. Motor yataklarında meydana gelen arızaları tespit etmek için yeni bir tek boyutlu konvolüsyonel sinir ağı modeli. Firat Univ J Eng Sci, 35: 669–678.
- Glowacz A, Sulowicz M, Zielonka J, Li Z, Glowacz W, Kumar A. 2025. Acoustic fault diagnosis of three-phase induction motors using smartphone and deep learning. Expert Syst Appl, 262: 125633.
- Kao IH, Wang WJ, Lai YH, Perng JW. 2018. Analysis of permanent magnet synchronous motor fault diagnosis based on learning. IEEE Trans Instrum Meas, 68: 310–324.
- Karabacak YE, Özmen NG. 2022. Rulmanlarda titreşim verilerinden durum izleme ve arıza teşhisi için derin öğrenme yönteminin uygulanması. Konya J Eng Sci, 10: 346–365.
- Kilic ME, Acar YE. 2024. Performance evaluation of the timefrequency transformation methods on electrical machinery fault detection. Bitlis Eren Univ J Sci, 13: 1147–1157.
- Liu W, Chen W, Zhang Z. 2020. A novel fault diagnosis approach for rolling bearing based on high-order synchrosqueezing transform and detrended fluctuation analysis. IEEE Access, 8: 12533–12541.
- Lopez-Perez D, Antonino-Daviu J. 2017. Application of infrared thermography to failure detection in industrial induction motors: Case stories. IEEE Trans Ind Appl, 53: 1901–1908.
- Mehta A, Goyal D, Choudhary A, Pabla B, Belghith S. 2021. Machine learning-based fault diagnosis of self-aligning bearings for rotating machinery using infrared thermography. Math Probl Eng, 2021: 9947300.
- Mueller PN, Woelfl L, Can S. 2023. Bridging the gap between AI and the industry—a study on bearing fault detection in PMSM-driven systems using CNN and inverter measurement. Eng Appl Artif Intell, 126: 106834.
- Nayana B, Geethanjali P. 2017. Analysis of statistical timedomain features effectiveness in identification of bearing faults from vibration signal. IEEE Sens J, 17: 5618–5625.
- Pacheco-Cherrez J, Fortoul-Diaz JA, Cortes Santacruz F, Aloso Valerdi LM, Ibarra Zarate DI. 2022. Bearing fault detection with vibration and acoustic signals: Comparison among different machine learning classification methods. Eng Fail Anal, 139: 106515.
- Qiao M, Yan S, Tang X, Xu C. 2020. Deep convolutional and LSTM recurrent neural networks for rolling bearing fault diagnosis under strong noises and variable loads. IEEE Access, 8: 66257–66269.
- Sabir R, Rosato D, Hartmann S, Gühmann C. 2019. LSTM based bearing fault diagnosis of electrical machines using motor current signal. In: Proceedings of 18th IEEE International Conference on Machine Learning and Applications, December 16–19, Boca Raton, USA, pp: 613–618.
- Seflek I, Acar YE, Yaldiz E. 2020. Small motion detection and non-contact vital signs monitoring with continuous wave Doppler radars. Elektron Elektrotech, 26: 54–60.
- Smith WA, Randall RB. 2015. Rolling element bearing diagnostics using the Case Western Reserve University data: A benchmark study. Mech Syst Signal Process, 64: 100–131.
- Zhang S, Zhang S, Wang B, Habetler TG. 2020a. Deep learning

algorithms for bearing fault diagnostics—A comprehensive review. IEEE Access, 8: 29857–29881.

Zhang Y, Xing K, Bai R, Sun D, Meng Z. 2020b. An enhanced convolutional neural network for bearing fault diagnosis

based on time-frequency image. Measurement, 157: 107667. Zhu Z, Lei Y, Qi G, Chai Y, Mazur N, An Y, Huang X. 2023. A review of the application of deep learning in intelligent fault diagnosis of rotating machinery. Measurement, 206: 112346.